Investigation of Ligand Binding and Protein Dynamics in *Bacillus subtilis* Chorismate Mutase by Transverse Relaxation Optimized Spectroscopy−Nuclear Magnetic Resonance[†,‡]

Alexander Eletsky,[§,||] Alexander Kienhöfer,[§] Donald Hilvert, and Konstantin Pervushin*

Department of Chemistry and Applied Bioscience, Swiss Federal Institute of Technology, ETH Hönggerberg, 8093 Zürich, Switzerland

Received December 8, 2004; Revised Manuscript Received February 16, 2005

ABSTRACT: The structural and dynamical consequences of ligand binding to a monofunctional chorismate mutase from *Bacillus subtilis* have been investigated by solution NMR spectroscopy. TROSY methods were employed to assign 98% of the backbone $^{1}H^{N}$, $^{1}H^{\alpha}$, ^{15}N, $^{13}C'$, and $^{13}C^{\alpha}$ resonances as well as 86% of the side chain ^{13}C resonances of the 44 kDa trimeric enzyme at 20 °C. This information was used to map chemical shift perturbations and changes in intramolecular mobility caused by binding of prephenate or a transition state analogue to the X-ray structure. Model-free interpretation of backbone dynamics for the free enzyme and its complexes based on ^{15}N relaxation data measured at 600 and 900 MHz showed significant structural consolidation of the protein in the presence of a bound ligand. In agreement with earlier structural and biochemical studies, substantial ordering of 10 otherwise highly flexible residues at the C-terminus is particularly notable. The observed changes suggest direct contact between this protein segment and the bound ligand, providing support for the proposal that the C-terminus can serve as a lid for the active site, limiting diffusion into and out of the pocket and possibly imposing conformational control over substrate once bound. Other regions of the protein that experience substantial ligand-induced changes also border the active site or lie along the subunit interfaces, indicating that the enzyme adapts dynamically to ligands by a sort of induced fit mechanism. It is believed that the mutase-catalyzed chorismate-to-prephenate rearrangement is partially encounter controlled, and backbone motions on the millisecond time scale, as seen here, may contribute to the reaction barrier.

The monofunctional chorismate mutase from *Bacillus subtilis* (BsCM)[1] is a well-studied enzyme that catalyzes the rearrangement of chorismate to prephenate (Scheme 1), a key step in the biosynthesis of the aromatic amino acids tyrosine and phenylalanine. Extensive biochemical (*1*−*11*), structural (*12*−*14*), and computational (*15*−*31*) investigations suggest that the million-fold rate acceleration it achieves is brought about by constraining the flexible substrate in a high-energy, diaxial conformation and by stabilizing the chairlike pericyclic transition state electrostatically. How structural changes that accompany ligand binding might modulate catalytic efficiency is less clear.

Scheme 1

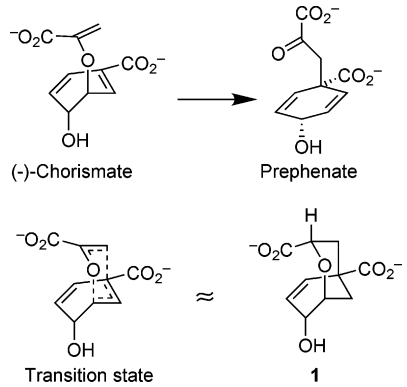

BsCM has been characterized crystallographically in the absence of ligands and as a complex with product and an endo-oxabicyclic transition state analogue [compound **1** (*32*)] (*12*−*14*). The 127-amino acid protein assembles as a homotrimer with overall pseudo-α/β-barrel topology. The three identical active sites are localized at the subunit interfaces. The side chains of residues Phe57, Ala59, Lys60, Val73, Thr74, and Cys75 from one subunit and Arg7′, Glu78′, Arg90′, Tyr108′, and Leu115′ from its neighbor are used to construct the binding pocket and provide numerous hydrophobic, hydrogen bonding, and ionic groups for molecular recognition. Of these, Arg90, Arg7, and Glu78 have been identified as being particularly important for catalysis

[†] This work was funded by the Swiss National Foundation and the ETH Zürich.

[‡] The NMR data have been deposited at BMRB (www.bmrb.wisc.edu) as entries 6494 (free form), 6495 (TSA complex), and 6496 (prephenate complex).

* To whom correspondence should be addressed: Department of Chemistry and Applied Bioscience, Swiss Federal Institute of Technology, ETH Hönggerberg, CH-8093 Zürich, Switzerland. Phone: +41-1-632-0922. Fax: +41-1-632-1021. E-mail: kope@phys.chem.ethz.ch.

[§] These authors contributed equally to this study.

[||] Current address: Department of Chemistry, University at Buffalo, 816 Natural Sciences Complex, Buffalo, NY 14260-3000.

[1] Abbreviations: BsCM, *B. subtilis* chorismate mutase; CSA, chemical shift anisotropy; FTIR, Fourier transform infrared; NMR, nuclear magnetic resonance; NOE, nuclear Overhauser effect; TOCSY, total correlation spectroscopy; TROSY, transverse relaxation optimized spectroscopy.

10.1021/bi0474259 CCC: $30.25
Published on Web 04/15/2005

(*4*−*10*). The guanidinium group of Arg90 interacts with the ether oxygen of the breaking C−O bond of chorismate in the transition state, Arg7 forms a salt bridge with the buried carboxylate of the enol pyruvate side chain, and Glu78 hydrogen bonds with the substrate hydroxyl group (*12*, *13*). The tertiary carboxylate groups of the bound inhibitor and bound prephenate are relatively solvent exposed at the entrance of the pocket, but potentially stabilizing contacts with the side chains of Arg63 and Arg116 are seen in some subunits (*13*) and may be important for inhibitor binding (*11*) and catalysis (*22*, *25*, *26*).

Although the overall structure of BsCM is similar in the liganded and unliganded states, ligand-induced conformational changes have been detected crystallographically (*13*) and by Fourier transform infrared (FTIR) spectroscopy (*3*). For instance, the original X-ray studies showed that much of the C-terminus, which is immediately adjacent to the active site but disordered in the absence of ligand, becomes substantially more ordered upon formation of the complex (*13*). The inherent flexibility of the tail segment in the free enzyme is also evident in a high-resolution structure obtained at high ionic strength and low pH (*14*), where it adopts a different conformation in each subunit of the trimer despite its involvement in crystal packing interactions. The relatively slow binding of substrate and dissociation of product, which partially limit the catalytic reaction (*1*, *8*), have been attributed to these structural changes (*3*, *13*). Selection experiments with randomly truncated BsCM variants have provided direct biochemical evidence for the contribution of the C-terminal tail to catalytic efficiency (*33*). Thus, although the last five residues of the protein can be removed without significantly altering the kinetic parameters, further truncations lead to substantial decreases in k_{cat}/K_m, due largely to increases in K_m (*33*, *34*). When 12 or more amino acids are trimmed from the C-terminus, inactive enzymes are obtained. The C-terminal 3_{10}-helix, formed by residues 111−115, is apparently required for a functional catalyst, even though the sequence of this segment is relatively tolerant to mutation (*33*). Additional residues beyond Leu115 presumably enhance ligand affinity by providing additional stabilizing contacts with the substrate and transition state.

To gain more insight into structural changes in BsCM, we have initiated NMR studies of the enzyme in the presence and absence of prephenate and compound **1**. In contrast to X-ray methods, which provide a rather static picture of the protein, NMR analysis can yield valuable information about the dynamic properties of the enzyme under native conditions (*35*, *36*). Although trimeric BsCM is rather large by NMR standards (44 kDa), we have successfully assigned nearly all of the backbone $^1H^N$, $^1H^\alpha$, ^{15}N, $^{13}C'$, and $^{13}C^\alpha$ resonances and most of the side chain ^{13}C resonances in the unliganded protein, and have also identified diagnostic ligand-induced perturbations of the ^{15}N and ^1H spins. In conjunction with ^{15}N relaxation measurements, which shed light on nanosecond and millisecond intramolecular motions of the backbone amide moieties, these data afford a comprehensive view of how the enzyme adapts dynamically to ligands in solution.

RESULTS

Assignment of Backbone Resonances. Because of its large size, the BsCM homotrimer was characterized by TROSY−NMR (*37*). The protein is well behaved in solution at 20 °C, affording well-resolved spectra under all conditions that were examined. Data analysis was greatly facilitated by the symmetric nature of the structure, which resulted in degenerate resonances for all three subunits.

At first, standard procedures were employed for the sequence-specific assignment of backbone residues in the unliganded enzyme. Two-dimensional (2D) [^{15}N,^1H]-TROSY, three-dimensional (3D) [^{13}C]-constant time-[^{15}N,^1H]-TROSY-HNCA, and [^{15}N,^1H]-TROSY-HNCACB spectra were acquired with a uniformly ^2H-, ^{13}C-, and ^{15}N-labeled BsCM sample. Although 120 backbone spin systems are expected, only 91 were identified, 45 of which could be linked into 10 strip fragments and unambiguously assigned with the help of Mapper (*38*). Incomplete exchange of amide deuterons with protons when the protein was dissolved in H_2O might explain why more peaks were not observed with uniformly deuterated BsCM. Similar results have been obtained with other large proteins expressed in D_2O (*39*, *40*), as a consequence of amide proton exchange rates for some residues on the order of months.

To overcome this problem, a partially deuterated sample [^2H (<35%)-, ^{13}C-, and ^{15}N-labeled BsCM] was prepared. NMR experiments involving constant time evolution in the ^{13}C dimension are unsuitable in this case because relaxation rates are too high at nonexchangeable sites due to the low deuterium content. We therefore employed a previously described strategy for assigning backbone resonances that combines sensitive 3D TROSY-HNCA (*41*) and TROSY-HNCO experiments with a 3D multiple-quantum HACACO experiment to detect $^{13}C'$ anti-phase coherence (*42*) and a 3D TROSY-HN(CA)HA experiment (*43*). The strong signals observed for the amides of C-terminal residues 118−127 and the moderate signals for residues Met2, Met77, and Asn124 in additional 3D TROSY-CBCA(CO)NH measurements proved to be useful for the assignment of residues Met77 and Asn124. Assignments were subsequently verified with ^{15}N-resolved TOCSY and NOESY spectra. Tentative NOE connectivities were checked for consistency with triple-resonance experiments. The availability of X-ray structural data for a large portion of the protein (residues 1−115) (*12*−*14*) facilitated this approach. The amide group of Arg7, which exhibits an unusual ^1H chemical shift of 11.9 ppm, was identified in [^{15}N,^1H]-TROSY and ^{15}N-resolved NOESY spectra and confirmed by 2D [^{13}C,^1H] versions of the same TROSY-HNCA and TROSY-HNCACB experiments with an increased proton spectral width (*44*).

Together, this suite of experiments allowed assignment of the resonances of all backbone amides of BsCM, except those of Gly67 and Gly83, which were not found in the [^{15}N,^1H]-TROSY spectra. In the X-ray structure of the enzyme (*12*−*14*), these residues are situated in loop regions, so their resonance lines might be broadened by conformational exchange. Nearly complete assignment of the aliphatic side chain ^{13}C and ^1H resonances using carbon-detected TOCSY experiments was recently reported (*45*).

The backbone amides of the BsCM complexes with prephenate and inhibitor **1** were assigned on the basis of NOE connectivities in the ^{15}N-resolved NOESY spectra. Assignments from unliganded BsCM were taken as a starting point, and assuming a basic similarity of backbone conformations, the corresponding spin systems for the liganded forms of

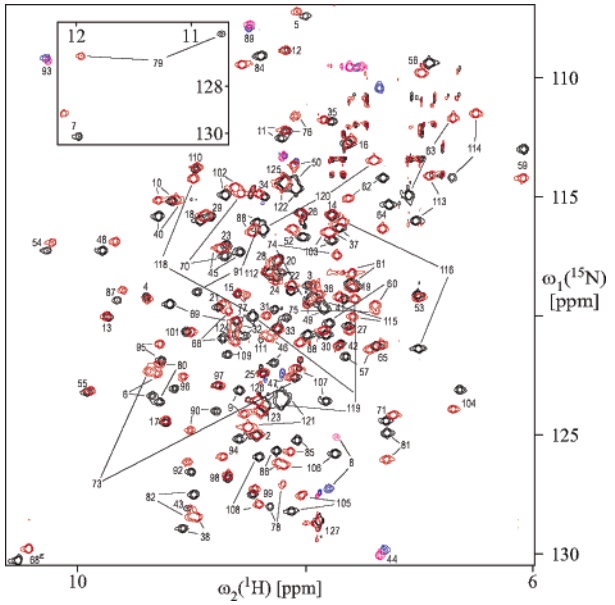

FIGURE 1: Superposition of $^1H-^{15}N$ TROSY spectra for BsCM (black positive contours and blue negative) and the BsCM·**1** complex (red positive contours and magenta negative). The residue-specific assigned peaks are labeled according to the respective residue number in the protein sequence. The cross-peaks stemming from the side chain groups are unlabeled.

BsCM were identified. This approach allowed all backbone amide ^1H and ^{15}N resonances except those associated with Gly67 and Gly83 to be assigned. TROSY-HNCA spectra of the ^{15}N-, ^{13}C-, and ^2H (50%)-labeled BsCM·**1** complex confirmed the assignments. The assigned [^{15}N,^1H]-TROSY spectra of free BsCM and the BsCM·**1** complex are superimposed in Figure 1. The ^1H and ^{15}N chemical shifts for the free enzyme and the prephenate and transition state analogue complexes are compared in pairwise fashion in Figure 2.

Ligand Binding. Prephenate binding was monitored by TROSY spectroscopy using uniformly ^2H- and ^{15}N-labeled BsCM. When roughly 50% of the binding sites are occupied [$K_D = 70\ \mu M$ (*1*)], an intermediate exchange regime applies. As a consequence, most of the peaks with a line separation of <150 Hz in at least one dimension were broadened beyond the detection limit. Increasing the concentration of prephenate saturates the enzyme and effectively eliminates this exchange broadening to give well-resolved spectra. These results are in qualitative agreement with the reported dissociation constant k_{off} of 270 s^{-1} at 25 °C (*2*).

In contrast, the free and ligand-bound states of the BsCM·**1** complex [$K_D = 1.2\ \mu M$ (*10*)] are found to be in slow exchange on the chemical shift time scale at 50% occupancy. Two cross-peaks corresponding to these two states are observed without significant broadening in TROSY spectra if their separation exceeds 30 Hz in at least one dimension. These cross-peaks collapse when the separation is less than 30 Hz. These observations suggest that k_{off} for the inhibitor is on the order of 10 s^{-1}.

^{15}N T_1, T_2, and HNOE Data. The ^{15}N relaxation rates measured at 600 and 900 MHz (Figure 4) were determined by nonlinear least-squares fitting of the magnetization decay curves to a single-exponential function. The maximum errors in T_1 and T_2 were obtained by a Monte Carlo-type procedure, which involved fitting of the intensity decay multiple times with random addition or subtraction of 5% of the measured peak volumes. The estimated averaged errors are 4 and 6% for the T_1 data and 8 and 10% for the corresponding T_2 data at both magnetic fields for BsCM and the BsCM·**1** complex, respectively, and thus amount to approximately 2.5 times the corresponding average standard errors. The estimated Monte Carlo errors for the $^{15}N\{^1H\}$ NOEs are ca. 10%.

Anisotropy and global rotational correlation times were evaluated with the symmetric top model (*46*). We used the R2R1_Diffusion program to determine whether diffusion anisotropy contributes significantly to the relaxation rates, following the approach of Tjandra et al. (*47*). T_1/T_2 ratios determined at two different fields for each protein form were evaluated independently. The principal moments of inertia tensors were calculated from protein atoms of representative trimers in the X-ray structures of unliganded BsCM and the BsCM·**1** complex (PDB entries 2CHS and 2CHT) with PDBinertia (http://cpmcnet.columbia.edu/dept/gsas/biochem/labs/palmer/software/diffusion.html). These moments are (1.00, 0.91, 0.91) and (1.00, 0.91, 0.89) for free BsCM and the BsCM·**1** complex, respectively, indicative of a slight axial anisotropy. The same BsCM trimers aligned with their tensors of inertia were used to obtain directional cosines of the amide bond vectors. Only data from residues with HNOE values greater than 0.65, and T_2 values within one standard deviation of the average, were considered. In the symmetric top approximation, the axis of symmetry is assumed to be the longest principal axis of inertia, which has the largest diffusion coefficient. The resulting global diffusion parameters are listed in Table 1. Calculated probabilities demonstrate that the anisotropic motional model (symmetric top) is statistically significant for BsCM. Furthermore, the orientation of the experimentally determined diffusion tensor matches that of the inertia tensor with a precision of a couple degrees. Although anisotropic diffusion is statistically less significant for the inhibitor complex, probably because of the somewhat lower precision of the measured relaxation rates or to global structural changes in the enzyme upon complexation, the relaxation data from both forms of the protein were analyzed using the anisotropic symmetric top model. This approach is justified by the observation that slight anisotropy has very little influence on the motional parameters of individual residues (*48*, *49*).

The average global correlation times determined from the T_1/T_2 ratios, which are the same for both protein forms, exhibit a marked field dependence (Table 1). This apparent field dependence indicates that the standard $\{S^2, t_e\}$ model with the approximation of fast internal dynamics ($t_e \ll \tau_M$) does not hold. Consequently, simultaneous fitting of global correlation times and model-free parameters of internal dynamics are required (*50*). Figure 5 shows values of the global target function χ^2 calculated for a range of correlation times (τ_M) using the extended $\{S_s^2, S_f^2, t_s\}$ model of the Model-Free approach applied only to the rigid part of the protein. In the absence of the R_{ex} term and assuming isotropic tumbling, there are $3n + 1$ unknowns for n sites and $5n$ observables (T_1 and T_2 at two magnetic fields and HNOE at one magnetic field). Because the HNOE values for this large protein measured at 600 MHz are largely independent of τ_M, the number of informative observables is reduced to $4n$, which exceeds the number of unknowns and ensures adequate determination of the model. It was previously

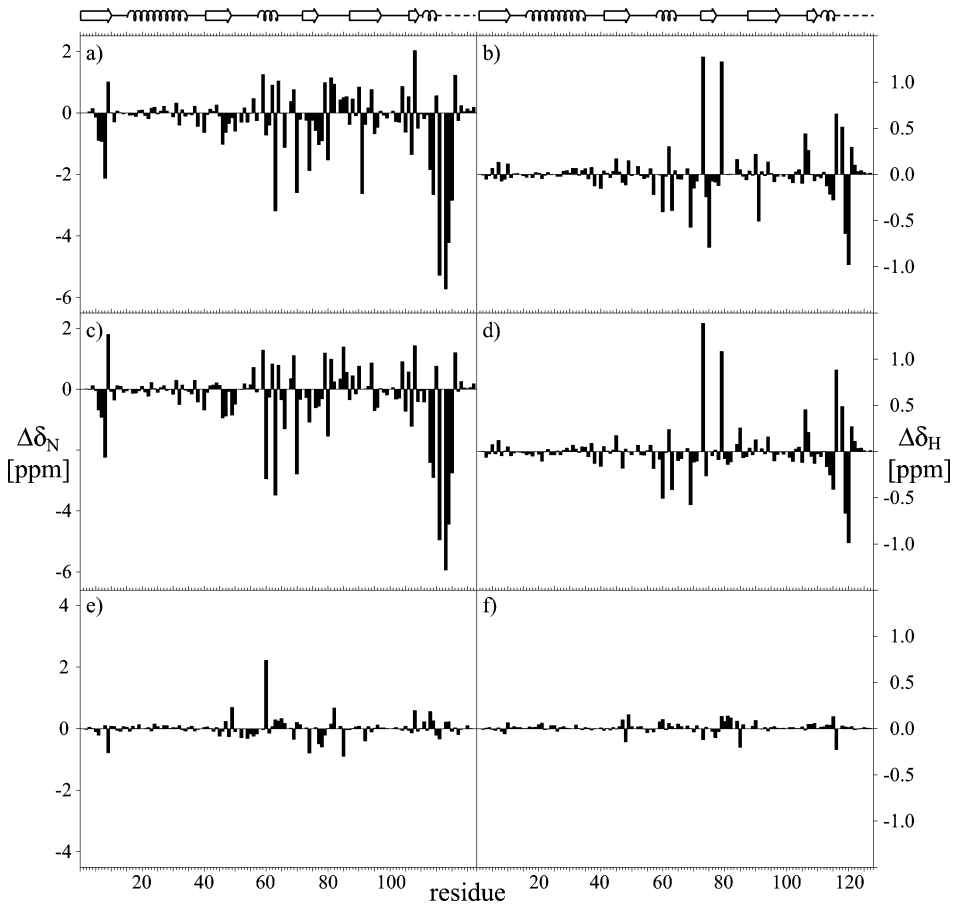

FIGURE 2: Comparison of backbone amide ^{1}H (a, c, and e) and ^{15}N (b, d, and f) chemical shifts for BsCM and its complexes with compound **1** and prephenate. (a and b) Chemical shift differences between the BsCM·**1** complex and unliganded BsCM. (c and d) Chemical shift differences between the BCM·prephenate complex and unliganded BsCM. (e and f) Chemical shift differences between the BsCM·**1** and BsCM·prephenate complexes.

demonstrated that above a certain value of τ_M, χ^2 levels off and a further increase in τ_M is offset by a decrease in S_s^2 (*51*). Consequently, although most BsCM residues are best described by the extended model (see below), the global correlation time cannot be determined in a manner that is independent of S_s^2. Using the criterion that χ^2 levels off as a function of τ_M, the global correlation time τ_M for the model-free analysis was estimated to be 37 ns.

Model-free analysis of the relaxation data is potentially complicated by uncertainty regarding the contribution of chemical shift anisotropy (CSA) to the observed T_1 and T_2 values (*52*). The constant CSA contribution to ^{15}N relaxation is field-dependent and can be large. For example, for an N−H vector tumbling with an isotropic correlation time of 37 ns, $S_f^2 = 0.85$, $S_s^2 = 0.85$, $t_s = 1$ ns, and an H−N bond length of 0.102 nm, an ^{15}N CSA value of −160 ppm would contribute approximately 22 and 40% to the observed ^{15}N T_1 at 600 and 900 MHz, respectively. Thus, the CSA relaxation mechanism must be considered explicitly for amide ^{15}N signals at fields higher than ca. 600 MHz. The variability of ^{15}N CSA at different sites of the protein, which can be as large as ±15 ppm (*53*), may also influence the statistical significance of the selected isotropic/anisotropic model. However, the absolute value of the order parameters is less important for the current investigation than the relative changes induced upon ligand binding. These differences are significantly less susceptible to variation of many model-free parameters, including ^{15}N CSA.

Model-Free Analysis of Intramolecular Backbone Mobility. The entire data set was analyzed using the symmetrical top model with the longest τ_M equal to 37 ns and $D_\parallel/D_\perp$ equal to 1.2. The applicability of the standard $\{S^2, t_e\}$ and extended $\{S_s^2, S_f^2, t_s\}$ models of the Model-Free approach was assessed on a residue-per-residue basis employing the *F*-test criterion (*54*). Calculations demonstrate that the relaxation rates of 30 residues in BsCM and 35 residues in the BsCM·**1** complex are described well by the standard model, but the extended model is required for the rest of the protein based on the 10% probability cutoff level of the *F*-test. In general, selection of an overly simple model of internal motions leads to overestimation of the generalized order parameters and underestimation of internal correlation times (*55*). Because of the relatively small number of residues described by the standard model, and their scattered distribution over the protein sequence, we consequently applied the extended model uniformly to the entire enzyme. This procedure simplifies cross comparison of changes in intramolecular dynamics by providing the same dynamical model for the residues in both structural forms of the protein.

The *F*-test criterion was subsequently employed to distinguish between $\{S_s^2, S_f^2, t_s\}$ and $\{S_s^2, S_f^2, t_s, R_{ex}\}$ models. At a probability cutoff of 10%, the number of residues requiring the R_{ex} term was 30 in BsCM and 18 in the BsCM·**1** complex. Figure 6 shows that there is a correlation between S_s^2 and the secondary structure. The regions of low S_s^2 values around Arg14, Thr50, and Ser66 in both liganded and

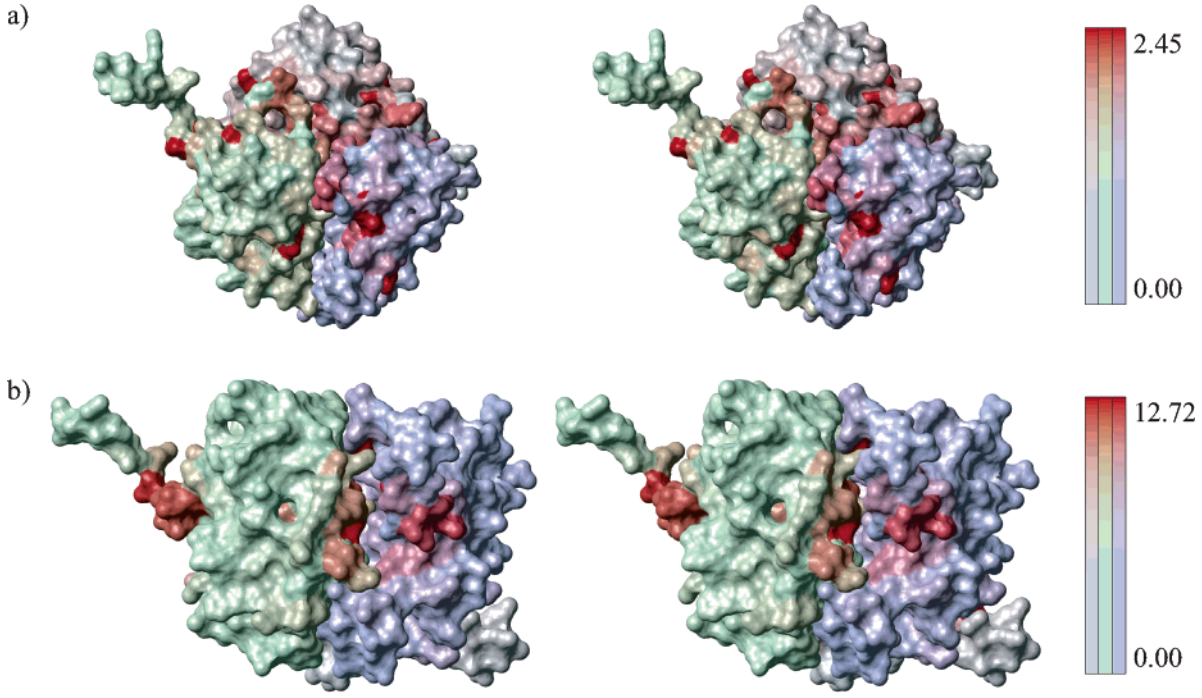

FIGURE 3: Stereoviews of BsCM with chemical shift differences mapped onto the 1.3 Å X-ray structure obtained at low pH and high ionic strength (*14*) (PDB entry 1DBF) as a model. The individual subunits are colored gray, green, and blue. The red hue is proportional to the quadratic mean $\sqrt{(\Delta\sigma_N)^2+(10\Delta\sigma_H)^2}$. (a) Comparison of the BsCM·**1** and BsCM·prephenate complexes. (b) Comparison of free BsCM and the BsCM·**1** complex.

unliganded forms correspond to loops in the structure. Other loops do not show significant conformational mobility on the nanosecond time scale. Correlation between crystallographic *B*-factors and S_s^2 is less pronounced (Figure 6). There are several regions characterized by high *B*-factor values, but only those around Arg14 and Leu66 also have low S_s^2 values. The order parameter for motions on the picosecond time scale, S_f^2, remains high throughout the sequence, declining slightly toward the C-terminus. The correlation time for internal motions, t_s, falls generally in the range of 1−3 ns, as observed for other proteins, and decreases slightly at the C-terminus (data not shown).

DISCUSSION

Nearly all the backbone $^1H^N$, $^1H^\alpha$, ^{15}N, $^{13}C'$, and $^{13}C^\alpha$ resonances and most of the side chain ^{13}C resonances in the unliganded BsCM homotrimer have been successfully assigned. Secondary structure elements in the protein were identified by chemical shift analysis of the $^1H^\alpha$, ^{13}CO, $^{13}C'$, and $^{13}C^\alpha$ spins using CSI (*56*), and confirmed with data from ^{15}N-resolved NOESY-TROSY spectra. Generally good agreement was observed between the NMR and X-ray data regarding the locations of the five β-strands and three helices in each subunit. Differences include a somewhat shorter β-strand II than is observed crystallographically, which may be attributed to the fact that Val42 and Val43 form a β-bulge instead of the standard β-sheet seen in the X-ray structures (*12*, *13*). In addition, the chemical shift index indicates that the second helix is shorter by one residue than in the X-ray structures (residues 58−63 vs 58−64), and predicts a coiled conformation for residues 111−115 rather than a 3_{10}-helix.

Of all the assigned backbone amides, the $^1H^N$ resonances of Arg7 and Met79 show unusually large deviations from random coil values (∼3−4 ppm) (Figure 1). Calculations with MOLMOL (*57*) based on the X-ray structures of BsCM indicate that ring current effects cannot account for these anomalies. Instead, the large Arg7 chemical shift has been attributed to a strong hydrogen bond with the $N^{\delta1}$ atom of His106 (*44*). This same hydrogen bond is also observed in the structure of a related chorismate mutase from *Thermus thermophilus* (PDB entry 1ODE) (*58*), which shares only 47% sequence identity with BsCM, suggesting that it is a conserved feature in this enzyme class. The backbone amide proton of Met79 is hydrogen bonded to the carboxylate group of Glu78 (*12*, *13*). The latter is a key active site residue, and this interaction may be important for positioning the carboxylate for effective catalysis.

Regions of the protein influenced by ligand binding are readily apparent when the chemical shifts obtained for the unliganded trimer are compared with those for the product and transition state analogue complexes (Figure 2). It is known from X-ray studies that prephenate and compound **1** make similar contacts with the enzyme active site (*12*, *13*), so it is not surprising that their respective complexes exhibit only small chemical shift differences (compare panels e and f of Figure 2). Those differences that are observed are distributed nonrandomly in the 3D structure, and are generally localized at the active site (Figure 3a), reflecting the different structures of the ligands and possibly subtle dissimilarities in their binding modes. Much larger chemical shift differences are seen when either of these complexes is compared with the unliganded enzyme (compare panels a and b or panels c and d of Figure 2). The largest effects are associated with three regions of the protein: (i) residues 6−9 in β-strand I, (ii) a long stretch extending from residue 57 to 80, covering the second helix of the enzyme and β-strand

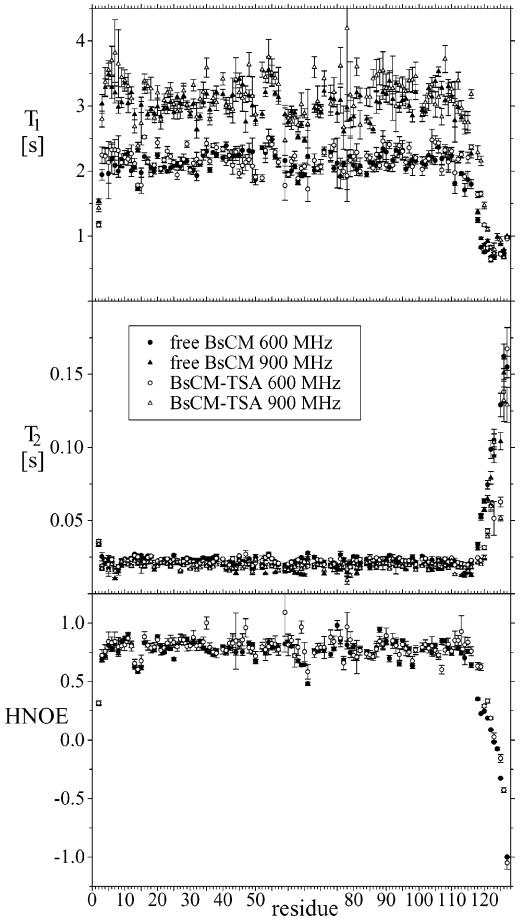

FIGURE 4: Experimental ^{15}N T_1, T_2, and HNOE data. Values of T_1, T_2, and HNOE at 600 MHz (for ^{1}H) polarizing field strength are represented by circles. ^{15}N T_1 and T_2 data at 900 MHz are represented by triangles. Filled and empty symbols stand for BsCM and the complex with transition state analogue **1**, respectively. Due to low cross-peak intensities and spectral overlap, relaxation data are not available for Ile32, Leu47, Leu85, Glu110, and Asn124 in the unliganded enzyme and for Cys75, Asn124, Thr122, and Thr125 in the BsCM·**1** complex. Residues Gly67 and Gly83, which were not found in the TROSY spectra, were not assigned.

Table 1: Anisotropic Rotational Diffusion Parameters

	BsCM		BsCM·**1**	
	600 MHz	900 MHz	600 MHz	900 MHz
$D_\parallel/D_\perp$	1.16 ± 0.04	1.27 ± 0.05	0.91 ± 0.06	1.07 ± 0.07
τ_m (ns)[a]	31.2 ± 0.2	27.1 ± 0.1	31.6 ± 0.2	27.2 ± 0.1
θ (deg)	1.5 ± 0.1	1.1 ± 0.1	1.3 ± 0.2	0.0 ± 0.3
φ (deg)	1.3 ± 0.1	1.4 ± 0.1	6.0 ± 0.2	4.3 ± 7.6
F-value	7.06	5.52	2.08	1.03
P(*F*)	0.0003	0.0017	0.11	0.38

[a] The error associated with the τ_m values was calculated using the statistical root-mean-square deviation of T_2/T_1 ratios for individual amino acids.

III, and (iii) C-terminal residues 106−121 (Figures 2 and 3). When these differences are mapped onto a 3D model of the enzyme (Figure 3b), it is evident that the active sites, the subunit interfaces, and the C-terminal tails experience the largest ligand-induced perturbations.

As might be expected, many active site residues, including Arg7, Phe57, Glu78, and Arg90, are sensitive to ligand binding. The moderate chemical shift changes that are observed presumably reflect small adjustments in residue

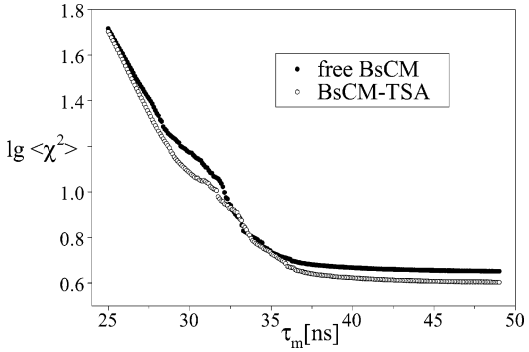

FIGURE 5: Grid search on τ_M. Dependence of the target function on the global correlation time τ_M when the extended model for internal dynamics is employed.

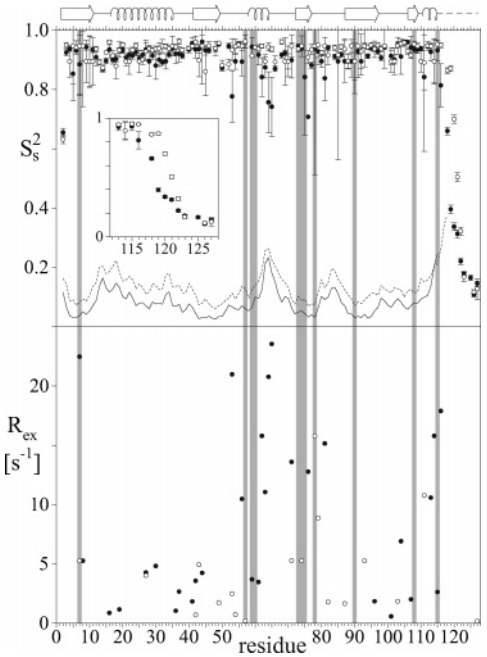

FIGURE 6: Slow motion order parameter S_s^2 and exchange terms obtained in the Model-Free analysis using the extended model for free BsCM (●) and the BsCM·**1** complex (○). Gray stripes denote active site residues according to ref *13*. *B*-Factors of backbone nitrogen atoms in the X-ray structures of free BsCM (2CHS) and the BsCM·**1** complex (2CHT) are represented by a solid line and a dashed line, respectively. A schematic representation of the secondary structure is shown at the top.

positioning or the altered molecular environment of the active site in the presence of ligand. By comparison, Arg63 and Arg116 exhibit considerably larger effects, consistent with crystallographic data showing that their relatively flexible side chains are recruited to the active site to bind the tertiary carboxylate of prephenate or the transition state analogue (*12*, *13*). Although hysteresis has not been observed in the binding or kinetic properties of the enzyme, minor adjustments at the trimer interfaces are likewise unsurprising. These perturbations indicate global conformational rearrangements of the trimer upon complexation.

Interestingly, the amide signals of Val73 and Met79, which are near the active site but do not contact the ligand directly, are among the residues most strongly affected by the presence of a ligand. As noted above, the Met79 amide helps to position the carboxylate side chain of Glu78, which in turn provides a key hydrogen bonding interaction with the alcohol group of both prephenate and **1**. The chemical shift change

Table 2: Kinetic Parameters for BsCM and Several C-Terminally Truncated Variants[a]

	k_{cat} (s^{-1})	K_m (μM)	k_{cat}/K_m (M^{-1} s^{-1})
wild-type BsCM[b]	46 ± 3	67 ± 5	6.9×10^5
BsCM(1−124)[c]	33 ± 2	71 ± 10	4.6×10^5
BsCM(1−122)[c]	84 ± 5	140 ± 15	6.0×10^5
BsCM(1−121)[c]	70 ± 6	230 ± 40	3.0×10^5
BsCM(1−120)[d]	44 ± 5	1010 ± 130	4.3×10^4
BsCM(1−119)[c]	65 ± 1	920 ± 23	7.1×10^4
BsCM(1−116)[b]	28 ± 7	9600 ± 3000	2.9×10^3

[a] Enzymes were assayed in 50 mM potassium phosphate buffer (pH 7.5) at 30 °C. [b] From ref *33*. [c] From this work. [d] From ref *34*.

in this case likely reflects the altered hydrogen bonding network that arises when the ligand binds (*12*, *13*). The sensitivity of the Val73 amide may be due to the fact that it is solvated by water in the free enzyme, but proximal to the positively charged guanidinium group of Arg116 in the complex (*13*).

The most dramatic ligand-induced perturbations in BsCM are associated with amino acids at the C-terminus, starting at residue 106, immediately before the last β-strand, and extending beyond the final 3_{10}-helix to residue 121. This stretch includes two active site residues, Tyr108 and Leu115, which interact with the enol pyruvate side chain of the substrate. Several residues beyond Leu115, especially Arg116, Asp118, Leu119, and Ser120, experience some of the largest chemical shift changes in the entire protein. The latter are the same residues that become more ordered crystallographically in response to a ligand (*13*). These amino acids apparently serve as a hinge between the 3_{10}-helix (residues 111−115) and the essentially unstructured terminus (Figure 3). Rigidification of this segment contributes to the organization of the active site and may also facilitate recruitment of the Arg116 side chain for carboxylate recognition. Proteins truncated in this region, while active, exhibit substantial increases in K_m (Table 2), indicative of a loss of productive binding interactions. In contrast, residues beyond Leu121 are unimportant for binding; negligible chemical shift differences are observed in this region, consistent with the observation that the last six amino acids of the protein can be deleted without appreciably affecting activity (*33*).

Direct information about backbone flexibility over a broad range of time scales can be gleaned from ^{15}N relaxation data (*53*, *59*). In Figure 4, T_1, T_2, and HNOE data for the free enzyme and its complex with the transition state analogue **1** are compared. Interpretation of the relaxation data using the so-called "Model-Free" approach of Lipari and Szabo (*60*, *61*) provides tangible insight into how ligand binding influences the amplitudes and time scales of backbone motions. This method assesses "fast" internal motions (faster than the overall tumbling, i.e., pico- to nanosecond dynamics) using two parameters at each site that are independent of the motional model. These parameters are the generalized order parameter, S^2, which measures the spatial restriction of the internal motion, and the effective local correlation time, t_e, which correlates with the rate of internal or local motion. Coupling the numerical values of S^2 and t_e with a physically reasonable model allows the complex intramolecular motions of the macromolecule to be described (*46*). For the current study, it suffices to note that values of S^2, which describe nanosecond events, vary from 0 to 1, with the two extremes corresponding to fully flexible and fully rigid molecular segments, respectively. The original Model-Free approach was subsequently extended by incorporating local motions at two time scales, two associated order parameters, and the overall correlation time τ_c (*62*). In addition, it was realized that exchange broadening, R_{ex}, is not fully quenched in the experimental pulse sequences. The latter measures conformational diversity on the millisecond time scale, with larger values corresponding to greater diversity. In total, then, the extended formalism is parametrized by six variables: τ_c, t_s, t_f, S_s^2, S_f^2, and R_{ex}. Because the t_f and S_f^2 parameters have a rather uniform distribution throughout the BsCM sequence, as has been observed for several other proteins (*53*, *63*), we focus our discussion on ligand-induced changes in R_{ex} and S_s^2, which reflect changes in the intramolecular dynamics on the millisecond and nanosecond time scales, respectively.

As shown in Figure 6, the free enzyme requires more R_{ex} terms to reproduce the experimental relaxation data than does the transition state analogue complex, indicating that ligand binding induces structural consolidation on the millisecond time scale. For example, both forms of the enzyme require this term for residues Arg7, Leu27, Val42, Leu53, and Val71, whereas residues Gly8, Thr16, Glu19, Lys30, His36, Thr37, Asp41, Gln44, Val56, Ala61−Leu65, Met76, Val81, Gln96, Ile104, Val107, and Val113−Arg116 have significant R_{ex} values only in the free enzyme. Evidently, segments of the unliganded protein roughly corresponding to the second and third helices (i.e., residues 58−64 and 111−115, respectively), in addition to numerous isolated residues distributed over the entire primary sequence, have considerable internal mobility on the millisecond time scale that is substantially dampened upon ligand binding. Extensive dialysis of the samples to remove potential contaminants argues against transient binding of some chemical species at the active site as the origin of the observed exchange broadening in the free enzyme. The alternative possibility that exchange broadening is induced by motions of atomic groups that are spatially proximal but remote in sequence from the segments in question (*64*, *65*) also seems unlikely on structural grounds. However, it is striking that the two flexible helices flank the entrance to the active site, and that they either contain or are immediately adjacent to arginines (Arg63 and Arg116) whose side chains are disordered in the unliganded enzyme but involved in substrate recognition in the complex (*13*). Although less pronounced, the structural ordering inferred here is reminiscent of the ligand-induced conformational transition seen for an engineered mutase that undergoes a transition from a molten globular state to a well-folded protein upon ligand binding (*66*). In the case of BsCM, the observed structural changes are potentially significant for catalysis given that the rearrangement of chorismate to prephenate also proceeds on a millisecond time scale at the active site (46 s^{-1}).

Judging from the S_s^2 values (Figure 6), these same general regions also become more ordered in the nanosecond regime (Figure 7). In this case, the largest ligand-induced changes are associated with the C-terminal region, which is the least ordered part of the protein (Figure 6). The unliganded enzyme is relatively structured up to Arg116, one residue more than observed in the original crystal structure (*13*). Beyond this position, the order parameters gradually decrease

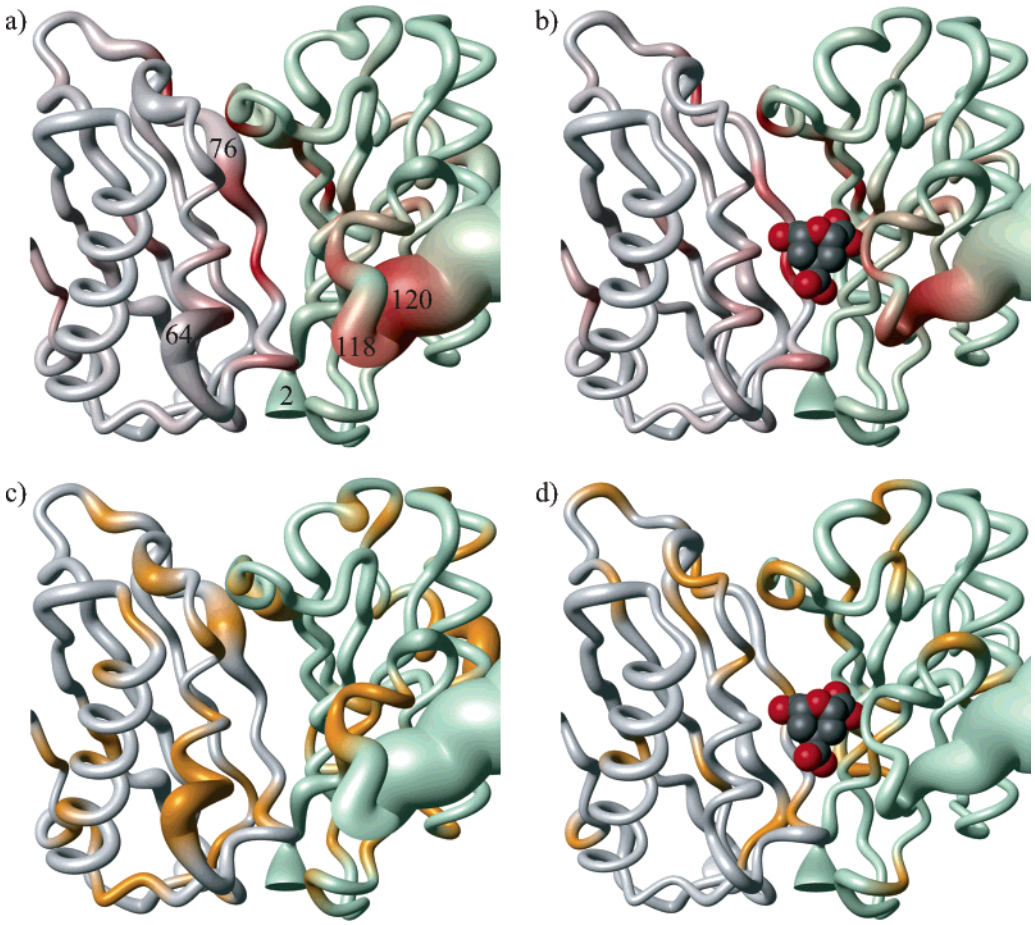

FIGURE 7: Backbone dynamics mapped onto the 3D structure of BsCM. The unliganded enzyme (PDB entry 1DBF) is shown in panels a and c, and the BsCM·**1** complex (PDB entry 2CHT) is shown in panels b and d. For the purposes of illustration, the missing C-terminal residues in the latter structure were artificially grafted to the two subunits shown using the unliganded structure as a model. The thickness of the backbone trace is proportional to $(1 - S_s^2)$. The chemical shift changes in panels a and b are color-coded as in Figure 3b. Residues showing exchange broadening are colored orange in panels c and d.

to a value of ca. 0.1, which corresponds to a largely unstructured polypeptide. In contrast, the BsCM·**1** complex is reasonably well ordered up to Leu119, again consistent with X-ray data showing additional electron density extending out to this residue in some of the monomers of the complex (*13*). The following amino acids become increasingly flexible up to position 124, where a similarly unstructured state is reached as in the free enzyme.

The TROSY data reported here provide a snapshot of the dynamic properties of BsCM, affording insight into ligand-induced changes that may be important for catalysis. Previous attention has focused primarily on the C-terminal tail of the enzyme, which becomes more ordered in the presence of ligands (*3*, *13*), possibly restricting the diffusion of small molecules into and out of the active site. It may also control the conformation and hence the reactivity of bound chorismate. Our NMR analysis confirms the ligand-induced ordering of this protein segment. In addition, the observed chemical shift changes and relaxation data highlight several other regions of the large trimeric enzyme that appear to adapt dynamically to the ligand. The transitions observed between a conformationally flexible active site in the absence of ligand to a more rigid structure in its presence imply an induced fit mechanism for the *B. subtilis* mutase. Further work will be needed to clarify in detail how the observed protein dynamics modulate ligand affinity and catalytic efficiency. In this context, valuable complementary information about backbone motion might be obtained by investigating the relaxation of spin groups other than the N−H vector, such as the C^{α}−CO vector (*64*, *67*, *68*).

MATERIALS AND METHODS

Protein Production. Labeled BsCM proteins were produced in bacterial strain KA13/pKET3-W (*8*, *69*, *70*). The cells were grown in 20 mL/L of 10× Bioexpress YBN medium (Cambridge Isotope Laboratories) in 1 L for the ^{15}N-labeled protein, 0.7× Silantes d(35%)CN medium in 0.5 L for the uniformly ^{15}N-, ^{13}C-, and ^{2}H (<35%)-labeled protein, and 5.5 g of solid Celtone dCN medium in 1.5 L for the uniformly ^{15}N-, ^{13}C-, and ^{2}H-labeled protein. The culture broth also contained 100 mL/L 10× M9 salts (pH 7.2), 122.5 mg/L $MgSO_4 \cdot 2H_2O$, 7.5 mg/L $CaCl_2 \cdot 2H_2O$, 5 mg/L thiamin·HCl, 1 mL/L 1000× AroP-Mix (4-hydroxybenzoic acid, 2,3-dihydroxybenzoic acid, and 4-amino-4-hydroxybenzoic acid, at 5 g/L each), and 75 mg/L ampicillin. This medium was supplemented with 0.44% (w/v) glucose for the ^{15}N-labeled protein. For uniformly ^{15}N-, ^{13}C-, and ^{2}H (50%)-labeled BsCM, 1 L of liquid Celtone d(50%)CN medium containing 5 mg/L thiamin-HCl, 1 mL/L 1000× AroP-Mix, and 75 mg/L ampicillin was used. Buffers were prepared with deionized H_2O for uniformly ^{15}N-labeled and uniformly ^{15}N-, ^{13}C-, and ^{2}H (<35%)-labeled samples, 50%

D_2O in deionized H_2O for the uniformly ^{15}N-, ^{13}C-, and ^{2}H (50%)-labeled sample, and pure D_2O for the uniformly ^{15}N-, ^{13}C-, and ^{2}H-labeled sample.

Protein production was initiated by inoculating a preculture of 5 mL of LB medium (150 μg/mL Amp) with a single colony of freshly grown KA13/pKET3-W and incubating it overnight at 37 °C and 230 rpm. The main culture, prepared from the desired medium, was inoculated with this preculture at a ratio of 500 to 1 and grown to an OD_{600} of ca. 1 ($\sim$10 h in H_2O and $\sim$20 h in D_2O). Protein production was induced by adding 10 mL of 50 mM IPTG per liter. After induction, cells were incubated for 24 h (48 h for D_2O-containing medium) at 30 °C and 250 rpm and then harvested. The uniformly ^{15}N-, ^{13}C-, and ^{2}H (<35%)-labeled sample and the uniformly ^{15}N-, ^{13}C-, and ^{2}H-labeled sample were treated with 1.5 mL of a rifampicin solution (0.1 mg/mL in MeOH) per liter 1 h after induction. Protein was isolated and purified as previously described (*69*). This procedure afforded 66 and 69 mg (first and second batch, respectively) of ^{15}N-labeled BsCM, 24.8 mg of ^{15}N-, ^{13}C-, and ^{2}H (<35%)-labeled BsCM, 42.5 mg of uniformly ^{2}H-, ^{15}N-, and ^{13}C-labeled BsCM, and 68 mg of ^{2}H (50%)-, ^{15}N-, and ^{13}C-labeled BsCM. For the production of the fully deuterated enzyme, the host cells were adapted for growth in D_2O in sequential precultures of 0% D_2O, 50% D_2O, and 100% D_2O before inoculation of the main culture.

Truncated Mutases. Genes for BsCM variants containing premature TAA stop codons were engineered as described for the truncated BsCM(1−120) (*34*). The encoded proteins were produced, purified, and characterized according to published protocols (*33*, *34*).

Sample Preparation. The proteins were dialyzed into 25 mM potassium phosphate buffer (pH 7.5) using Slide-A-Lyser cassettes, and 3% D_2O was added prior to data collection. The following samples were prepared: 500 μL of 4 mM uniformly ^{2}H-, ^{13}C-, and ^{15}N-labeled BsCM in a standard NMR tube; 500 μL of 2.4 mM ^{2}H (<35%)-, ^{13}C-, and ^{15}N-labeled BsCM in a standard NMR tube; 500 μL of 2.0 mM ^{15}N-labeled BsCM in a standard NMR tube; 300 μL of 3.0 mM ^{15}N-labeled BsCM and 4.5 mM inhibitor **1** in a Shigemi NMR tube; 300 μL of 3.0 mM uniformly ^{15}N-labeled BsCM and 1.3 mg of prephenate in a Shigemi NMR tube; 500 μL of 3 mM ^{15}N-, ^{13}C-, and ^{2}H (50%)-labeled BsCM and 3 mM inhibitor **1**. The BsCM·**1** and BsCM· prephenate complexes were prepared by stepwise addition of the ligand until the ratio of the complex to the free protein was greater than 100. For compound **1**, 10 μL aliquots of a 30 mM aqueous stock solution were added to generate the inhibitor complex. To obtain the product complex, solid chorismate, which was rapidly converted to prephenate in situ, was added in three portions of $\sim$0.2, $\sim$0.4, and $\sim$0.7 mg. Complex formation was monitored by recording short ($\sim$30 min) 2D [^{15}N, ^{1}H]-TROSY spectra.

NMR Spectroscopy. All NMR experiments were performed at 293 K on Bruker Avance 600 and Avance 900 spectrometers. NMR data were processed with PROSA (*71*) or XWINNMR (Bruker Biospin), and resulting spectra were analyzed with Xeasy (*72*). Chemical shift referencing was based on DSS (sodium 2,2-dimethyl-2-silapentane-5-sulfonate) as the internal reference for ^{1}H nuclei. Indirect referencing of ^{13}C and ^{15}N nuclei based on the gyromagnetic ratios was employed.

3D CT-TROSY-HNCA, TROSY-HNCACB (*73*, *74*), and TROSY-HNCA (*41*) measurements were used for backbone assignments. Interscan relaxation delays of 1 s were employed. Time domain data in the ^{13}C dimension of the TROSY-HNCA experiment were doubled by mirror-image linear prediction (*75*) prior to Fourier transformation. The ^{15}N-resolved NOESY-TROSY data sets of all samples were expanded to double size in t_1 by forward linear prediction before the Fourier transformation.

Relaxation measurements. T_2 was measured in refocused echo experiments. To suppress cross-correlated relaxation, SEDUCE decoupling was applied to amide proton spins during T_1 and T_2 relaxation periods. T_1 values for BsCM at 600 MHz were estimated by nonlinear exponential fitting of the spectral intensities measured with nine relaxation delays: 0.05, 0.1, 0.2, 0.4, 0.8, 1.2, 1.8, 2.5, and 3.5 s. T_2 values for BsCM were estimated at 600 MHz, with 10 points: 2, 4, 8, 16, 24, 32, 48, 64, 80, and 96 ms. T_1 values for BsCM were estimated at 900 MHz, with nine points: 0.1, 0.2, 0.4, 0.8, 1.2, 1.8, 2.5, 3.5, and 4.5 s. T_2 values for BsCM were estimated at 900 MHz, with eight points: 2, 4, 8, 16, 24, 32, 48, and 64 ms. T_1 values for the BsCM·**1** complex were estimated at 600 MHz, with 12 points: 0.02, 0.05, 0.08, 0.1, 0.2, 0.3, 0.5, 0.8, 1.0, 1.2, 1.5, and 2.0 s. T_2 values for the BsCM·**1** complex were estimated at 600 MHz, with 10 points: 2, 4, 8, 16, 24, 32, 48, 64, 80, and 96 ms. T_1 values for the BsCM·**1** complex were estimated at 900 MHz, with eight points: 0.2, 0.4, 0.8, 1.2, 1.8, 2.5, 3.5, and 4.5 s. T_2 values for the BsCM·**1** complex were estimated at 900 MHz, with eight points: 2, 4, 8, 16, 24, 32, 48, and 64 ms. HNOE was measured in separately acquired saturation and reference TROSY-type experiments (*76*). All experiments utilized an interscan relaxation delay of 7 s. Saturation of proton spins was applied in 4 s using a train of high-power ^{1}H 180° pulses applied in 30 ms intervals. HNOE was calculated as the ratio of maximum peak intensity. The errors in HNOE were calculated from the spectral noise by error propagation. Relative errors in T_1 and T_2 below 5% have been set to 5%.

Relaxation Analysis. Relaxation data were analyzed by the Model-Free approach (*60*, *61*) with ModelFree version 4.15 (*77*, *78*), using an H−N bond length of 0.102 nm and ^{15}N CSA of −160 ppm. Assuming overall isotropic motion, the standard model of Lipari and Szabo produces the following spectral density function

$$J(\omega) = \frac{2}{5}\left[\frac{S^2\tau_M}{1+\omega^2{\tau_M}^2} + \frac{(1-S^2)\tau}{1+\omega^2\tau^2}\right] \quad (1)$$

where $1/\tau = 1/\tau_M + 1/\tau_e$, τ_e is the effective correlation time of internal motions, and S^2 is the generalized order parameter, reflecting the degree of spatial restriction of internal motions. An extended model incorporates the higher-order approximation (*62*):

$$J(\omega) = \frac{2}{5}\left[\frac{S^2\tau_M}{1+\omega^2{\tau_M}^2} + \frac{({S_f}^2 - S^2)\tau_s'}{1+\omega^2\tau_s'^2} + \frac{(1-{S_f}^2)\tau_f'}{1+\omega^2\tau_f'^2}\right] \quad (2)$$

where $1/\tau_s' = 1/\tau_M + 1/\tau_s$ and $1/\tau_f' = 1/\tau_M + 1/\tau_f$. This model makes sense only when the internal motions occur on significantly different time scales, "slow" and "fast", that is

if $\tau_s \gg \tau_f$. In this case, the generalized order parameter S^2 can be factorized

$$S^2 = S_f^2 S_s^2 \quad (3)$$

S_f^2 and S_s^2 represent order parameters of fast and slow internal motions, respectively. This model converges to the standard model if $S_f^2 = 1$, $S_s^2 = 1$, or $\tau_f = \tau_s$.

There are special cases of the given models in which internal motions are considered very fast and corresponding correlation times, τ_e or τ_f, negligibly small. In this case, eq 1 becomes

$$J(\omega) = \frac{2}{5}\frac{S^2\tau_M}{1 + \omega^2\tau_M^2} \quad (4)$$

and eq 2 becomes

$$J(\omega) = \frac{2}{5}\left[\frac{S^2\tau_M}{1 + \omega^2\tau_M^2} + \frac{(S_f^2 - S^2)\tau_s'}{1 + \omega^2\tau_s'^2}\right] \quad (5)$$

If global tumbling is anisotropic but axially symmetric, the standard model correlation function is

$$J(\omega) = \frac{2}{5}\left[S^2\sum_{i=1}^{3}\frac{A_i\tau_i}{1 + \omega^2\tau_i^2} + \frac{(1 - S^2)\tau}{1 + \omega^2\tau^2}\right] \quad (6)$$

where $A_1 = 0.75 \sin^4 \alpha$, $A_2 = 3 \sin^2 \alpha \cos^2 \alpha$, $A_3 = (1.5 \cos^2 \alpha - 0.05)^2$, and α is the angle between the amide bond vector and the molecular symmetry axis. The global correlation times are as follows: $\tau_1 = (4D_{\|} + 2D_{\perp})^{-1}$, $\tau_2 = (D_{\|} + 5D_{\perp})^{-1}$, and $\tau_1 = (6D_{\perp})^{-1}$. The effective global correlation time $\tau_{M,eff} = (2D_{\|} + 4D_{\perp})^{-1}$, and $1/\tau = 1/\tau_{M,eff} + 1/\tau_e$. Again, if the internal motions are sufficiently fast, the last term vanishes.

The effects of exchange line broadening are taken into account in the form of an additive R_{ex} term

$$\frac{1}{T_2} = \frac{1}{T_2^*} + R_{ex} \quad (7)$$

This finally yields a set of internal motion models with different numbers of degrees of freedom, which we designate as $\{S^2\}$, $\{S^2, R_{ex}\}$, $\{S^2, \tau_e\}$, $\{S^2, \tau_e, R_{ex}\}$, $\{S_s^2, S_f^2, \tau_s\}$, $\{S_s^2, S_f^2, \tau_s, R_{ex}\}$, and $\{S_s^2, S_f^2, \tau_s, \tau_f\}$.

Quantitative description of internal motions requires prior knowledge of global motion. This, in turn, depends on the particular model of the internal motions. One has to make successive approximations of the internal dynamics to obtain a self-consistent picture. The simplest approximation is utilized in the method of determining τ_M based on the T_1/T_2 ratios (*79*). This method implicitly assumes very fast internal dynamics, i.e., the $\{S^2\}$ model, with sufficiently large order parameters for most of the protein. If the protein structure is known, the anisotropy of the rotational diffusion can be determined in a similar way (*47*). The validity of this assumption can be easily proven by checking whether T_1/T_2 ratios measured at two different field strengths lead to the same motional parameters. If more accurate estimates are necessary, they can be obtained using the standard $\{S^2, \tau_e\}$ model for selected amide spins. The extended $\{S_s^2, S_f^2, \tau_s\}$ model does not yield a well-defined minimum of penalty function and provides only an estimate of τ_M (*51*, *80*).

ACKNOWLEDGMENT

We are grateful to Silantes (Munich, Germany) for giving us the experimental Silantes d(35%)CN liquid medium used for preparing the d(35%)CN-labeled enzyme sample as a gift, and Dr. Rosalino Pulido for the synthesis of **1**.

REFERENCES

1. Gray, J. V., Golinellipimpaneau, B., and Knowles, J. R. (1990) Monofunctional chorismate mutase from *Bacillus subtilis*: Purification of the protein, molecular cloning of the gene, and overexpression of the gene product in *Escherichia coli*, *Biochemistry 29*, 376−383.
2. Rajagopalan, J. S., Taylor, K. M., and Jaffe, E. K. (1993) C-13 NMR studies of the enzyme product complex of *Bacillus subtilis* chorismate mutase, *Biochemistry 32*, 3965−3972.
3. Gray, J. V., and Knowles, J. R. (1994) Monofunctional chorismate mutase from *Bacillus subtilis*: FTIR studies and the mechanism of action of the enzyme, *Biochemistry 33*, 9953−9959.
4. Cload, S. T., Liu, D. R., Pastor, R. M., and Schultz, P. G. (1996) Mutagenesis study of active site residues in chorismate mutase from *Bacillus subtilis*, *J. Am. Chem. Soc. 118*, 1787−1788.
5. Kast, P., Hartgerink, J. D., AsifUllah, M., and Hilvert, D. (1996) Electrostatic catalysis of the Claisen rearrangement: Probing the role of Glu78 in *Bacillus subtilis* chorismate mutase by genetic selection, *J. Am. Chem. Soc. 118*, 3069−3070.
6. Kast, P., AsifUllah, M., and Hilvert, D. (1996) Is chorismate mutase a prototypic entropy trap? Activation parameters for the *Bacillus subtilis* enzyme, *Tetrahedron Lett. 37*, 2691−2694.
7. Kast, P., Tewari, Y. B., Wiest, O., Hilvert, D., Houk, K. N., and Goldberg, R. N. (1997) Thermodynamics of the conversion of chorismate to prephenate: Experimental results and theoretical predictions, *J. Phys. Chem. B 101*, 10976−10982.
8. Mattei, P., Kast, P., and Hilvert, D. (1999) *Bacillus subtilis* chorismate mutase is partially diffusion-controlled, *Eur. J. Biochem. 261*, 25−32.
9. Kast, P., Grisostomi, C., Chen, I. A., Li, S. L., Krengel, U., Xue, Y. F., and Hilvert, D. (2000) A strategically positioned cation is crucial for efficient catalysis by chorismate mutase, *J. Biol. Chem. 275*, 36832−36838.
10. Kienhöfer, A., Kast, P., and Hilvert, D. (2003) Selective stabilization of the chorismate mutase transition state by a positively charged hydrogen bond donor, *J. Am. Chem. Soc. 125*, 3206−3207.
11. Mandal, A., and Hilvert, D. (2003) Charge optimization increases the potency and selectivity of a chorismate mutase inhibitor, *J. Am. Chem. Soc. 125*, 5598−5599.
12. Chook, Y. M., Ke, H. M., and Lipscomb, W. N. (1993) Crystal structures of the monofunctional chorismate mutase from *Bacillus subtilis* and its complex with a transition-state analog, *Proc. Natl. Acad. Sci. U.S.A. 90*, 8600−8603.
13. Chook, Y. M., Gray, J. V., Ke, H. M., and Lipscomb, W. N. (1994) The monofunctional chorismate mutase from *Bacillus subtilis*: Structure determination of chorismate mutase and its complexes with a transition-state analog and prephenate, and implications for the mechanism of the enzymatic reaction, *J. Mol. Biol. 240*, 476−500.
14. Ladner, J. E., Reddy, P., Davis, A., Tordova, M., Howard, A. J., and Gilliland, G. L. (2000) The 1.30 Å resolution structure of the *Bacillus subtilis* chorismate mutase catalytic homotrimer, *Acta Crystallogr. D56*, 673−683.
15. Wiest, O., and Houk, K. N. (1995) Stabilization of the transition state of the chorismate prephenate rearrangement: An ab initio study of enzyme and antibody catalysis, *J. Am. Chem. Soc. 117*, 11628−11639.
16. Guo, H., Cui, Q., Lipscomb, W. N., and Karplus, M. (2003) Understanding the role of active-site residues in chorismate mutase catalysis from molecular-dynamics simulations, *Angew. Chem., Int. Ed. 42*, 1508−1511.
17. Guo, H., Cui, Q., Lipscomb, W. N., and Karplus, M. (2001) Substrate conformational transitions in the active site of chorismate mutase: Their role in the catalytic mechanism, *Proc. Natl. Acad. Sci. U.S.A. 98*, 9032−9037.

18. Marti, S., Andres, J., Moliner, V., Silla, E., Tunon, I., and Bertran, J. (2003) Preorganization and reorganization as related factors in enzyme catalysis: The chorismate mutase case, *Chem.—Eur. J. 9*, 984−991.
19. Marti, S., Andres, J., Moliner, V., Silla, E., Tunon, I., and Bertran, J. (2004) A comparative study of Claisen and Cope rearrangements catalyzed by chorismate mutase. An insight into enzymatic efficiency: Transition state stabilization or substrate preorganization? *J. Am. Chem. Soc. 126*, 311−319.
20. Hur, S., and Bruice, T. C. (2003) Just a near attack conformer for catalysis (chorismate to prephenate rearrangements in water, antibody, enzymes, and their mutants), *J. Am. Chem. Soc. 125*, 10540−10542.
21. Hur, S., and Bruice, T. C. (2003) The near attack conformation approach to the study of the chorismate to prephenate reaction, *Proc. Natl. Acad. Sci. U.S.A. 100*, 12015−12020.
22. Lee, Y. S., Worthington, S. E., Krauss, M., and Brooks, B. R. (2002) Reaction mechanism of chorismate mutase studied by the combined potentials of quantum mechanics and molecular mechanics, *J. Phys. Chem. B 106*, 12059−12065.
23. Lyne, P. D., Mulholland, A. J., and Richards, W. G. (1995) Insights into chorismate mutase catalysis from a combined QM/MM simulation of the enzyme reaction, *J. Am. Chem. Soc. 117*, 11345−11350.
24. Ranaghan, K. E., and Mulholland, A. J. (2004) Conformational effects in enzyme catalysis: QM/MM free energy calculation of the 'NAC' contribution in chorismate mutase, *Chem. Commun.*, 1238−1239.
25. Ranaghan, K. E., Ridder, L., Szefczyk, B., Sokalski, W. A., Hermann, J. C., and Mulholland, A. J. (2004) Transition state stabilization and substrate strain in enzyme catalysis: Ab initio QM/MM modelling of the chorismate mutase reaction, *Org. Biomol. Chem. 2*, 968−980.
26. Szefczyk, B., Mulholland, A. J., Ranaghan, K. E., and Sokalski, W. A. (2004) Differential transition-state stabilization in enzyme catalysis: Quantum chemical analysis of interactions in the chorismate mutase reaction and prediction of the optimal catalytic field, *J. Am. Chem. Soc. 126*, 16148−16159.
27. Hall, R. J., Hindle, S. A., Burton, N. A., and Hillier, I. H. (2000) Aspects of hybrid QM/MM calculations: The treatment of the QM/MM interface region and geometry optimization with an application to chorismate mutase, *J. Comput. Chem. 21*, 1433−1441.
28. Kangas, E., and Tidor, B. (2001) Electrostatic complementarity at ligand binding sites: Application to chorismate mutase, *J. Phys. Chem. B 105*, 880−888.
29. Crespo, A., Scherlis, D. A., Marti, M. A., Ordejon, P., Roitberg, A. E., and Estrin, D. A. (2003) A DFT-based QM-MM approach designed for the treatment of large molecular systems: Application to chorismate mutase, *J. Phys. Chem. B 107*, 13728−13736.
30. Guimaraes, C. R. W., Repasky, M. P., Chandrasekhar, J., Tirado-Rives, J., and Jorgensen, W. L. (2003) Contributions of conformational compression and preferential transition state stabilization to the rate enhancement by chorismate mutase, *J. Am. Chem. Soc. 125*, 6892−6899.
31. Strajbl, M., Shurki, A., Kato, M., and Warshel, A. (2003) Apparent NAC effect in chorismate mutase reflects electrostatic transition state stabilization, *J. Am. Chem. Soc. 125*, 10228−10237.
32. Bartlett, P. A., Nakagawa, Y., Johnson, C. R., Reich, S. H., and Luis, A. (1988) Chorismate mutase inhibitors: Synthesis and evaluation of some potential transition-state analogs, *J. Org. Chem. 53*, 3195−3210.
33. Gamper, M., Hilvert, D., and Kast, P. (2000) Probing the role of the C-terminus of *Bacillus subtilis* chorismate mutase by a novel random protein-termination strategy, *Biochemistry 39*, 14087−14094.
34. Wendt, S., McCombie, G., Daniel, J., Kienhöfer, A., Hilvert, D., and Zenobi, R. (2003) Quantitative evaluation of noncovalent chorismate mutase-inhibitor binding by ESI-MS, *J. Am. Soc. Mass Spectrosc. 14*, 1470−1476.
35. Downing, A. K. (2004) *Protein NMR Techniques*, 2nd ed., Vol. 278, University of Oxford Press, Oxford, U.K.
36. Philippopoulos, M., and Lim, C. (1999) Exploring the dynamic information content of a protein NMR structure: Comparison of a molecular dynamics simulation with the NMR and X-ray structures of *Escherichia coli* ribonuclease HI, *Proteins 36*, 87−110.
37. Pervushin, K., Riek, R., Wider, G., and Wüthrich, K. (1997) Attenuated T_2 relaxation by mutual cancellation of dipole-dipole coupling and chemical shift anisotropy indicates an avenue to NMR structures of very large biological macromolecules in solution, *Proc. Natl. Acad. Sci. U.S.A. 94*, 12366−12371.
38. Guntert, P., Salzmann, M., Braun, D., and Wüthrich, K. (2000) Sequence-specific NMR assignment of proteins by global fragment mapping with the program MAPPER, *J. Biomol. NMR 18*, 129−137.
39. Gardner, K. H., Zhang, X. C., Gehring, K., and Kay, L. E. (1998) Solution NMR studies of a 42 KDa *Escherichia coli* maltose binding protein β-cyclodextrin complex: Chemical shift assignments and analysis, *J. Am. Chem. Soc. 120*, 11738−11748.
40. Salzmann, M., Pervushin, K., Wider, G., Senn, H., and Wüthrich, K. (2000) NMR assignment and secondary structure determination of an octameric 110 kDa protein using TROSY in triple resonance experiments, *J. Am. Chem. Soc. 122*, 7543−7548.
41. Eletsky, A., Kienhöfer, A., and Pervushin, K. (2001) TROSY NMR with partially deuterated proteins, *J. Biomol. NMR 20*, 177−180.
42. Pervushin, K., and Eletsky, A. (2003) A new strategy for backbone resonance assignment in large proteins using a MQ-HACACO experiment, *J. Biomol. NMR 25*, 147−152.
43. Hu, K. F., Eletsky, A., and Pervushin, K. (2003) Backbone resonance assignment in large protonated proteins using a combination of new 3D TROSY-HN(CA)HA, 4D TROSY-HACANH and C-13-detected HACACO experiments, *J. Biomol. NMR 26*, 69−77.
44. Eletsky, A., Heinz, T., Moreira, O., Kienhöfer, A., Hilvert, D., and Pervushin, K. (2002) Direct NMR observation and DFT calculations of a hydrogen bond at the active site of a 44 kDa enzyme, *J. Biomol. NMR 24*, 31−39.
45. Eletsky, A., Moreira, O., Kovacs, H., and Pervushin, K. (2003) A novel strategy for the assignment of side-chain resonances in completely deuterated large proteins using C-13 spectroscopy, *J. Biomol. NMR 26*, 167−179.
46. Luginbuhl, P., and Wüthrich, K. (2002) Semi-classical nuclear spin relaxation theory revisited for use with biological macromolecules, *Prog. Nucl. Magn. Reson. Spectrosc. 40*, 199−247.
47. Tjandra, N., Feller, S. E., Pastor, R. W., and Bax, A. (1995) Rotational diffusion anisotropy of human ubiquitin from ^{15}N NMR relaxation, *J. Am. Chem. Soc. 117*, 12562−12566.
48. Hall, J. B., and Fushman, D. (2003) Characterization of the overall and local dynamics of a protein with intermediate rotational anisotropy: Differentiating between conformational exchange and anisotropic diffusion in the B3 domain of protein G, *J. Biomol. NMR 27*, 261−275.
49. Luginbuhl, P., Pervushin, K. V., Iwai, H., and Wüthrich, K. (1997) Anisotropic molecular rotational diffusion in ^{15}N spin relaxation studies of protein mobility, *Biochemistry 36*, 7305−7312.
50. Dellwo, M. J., and Wand, A. J. (1989) Model-independent and model-dependent analysis of the global and internal dynamics of cyclosporine-A, *J. Am. Chem. Soc. 111*, 4571−4578.
51. Orekhov, V. Y., Pervushin, K. V., Korzhnev, D. M., and Arseniev, A. S. (1995) Backbone dynamics of (1−71)bacterioopsin and (1−36)bacterioopsin studied by 2-dimensional ^{1}H-^{15}N NMR spectroscopy, *J. Biomol. NMR 6*, 113−122.
52. Schneider, D. M., Dellwo, M. J., and Wand, A. J. (1992) Fast internal main-chain dynamics of human ubiquitin, *Biochemistry 31*, 3645−3652.
53. Korzhnev, D. M., Billeter, M., Arseniev, A. S., and Orekhov, V. Y. (2001) NMR studies of Brownian tumbling and internal motions in proteins, *Prog. Nucl. Magn. Reson. Spectrosc. 38*, 197−266.
54. Mandel, A. M., Akke, M., and Palmer, A. G. (1995) Backbone dynamics of *Escherichia coli* ribonuclease-H1: Correlations with structure and function in an active enzyme, *J. Cell. Biochem.*, 29.
55. d'Auvergne, E. J., and Gooley, P. R. (2003) The use of model selection in the model-free analysis of protein dynamics, *J. Biomol. NMR 25*, 25−39.
56. Wishart, D. S., and Sykes, B. D. (1994) The ^{13}C chemical-shift Index: A simple method for the identification of protein secondary structure using ^{13}C chemical-shift data, *J. Biomol. NMR 4*, 171−180.
57. Koradi, R., Billeter, M., and Wüthrich, K. (1996) MOLMOL: A program for display and analysis of macromolecular structures, *J. Mol. Graphics 14*, 51−55.
58. Inagaki, E., Kuramitsu, S., Yokoyama, S., Miyano, M., and Tahirov, T. H. (2003) The crystal structure of chorismate mutase from *Thermus thermophilus*, direct submission to Protein Data Bank.

59. Palmer, A. G., Williams, J., and McDermott, A. (1996) Nuclear magnetic resonance studies of biopolymer dynamics, *J. Phys. Chem. 100*, 13293−13310.
60. Lipari, G., and Szabo, A. (1982) Model-free approach to the interpretation of nuclear magnetic-resonance relaxation in macromolecules. 1. Theory and range of validity, *J. Am. Chem. Soc. 104*, 4546−4559.
61. Lipari, G., and Szabo, A. (1982) Model-Free Approach to the interpretation of nuclear magnetic-resonance relaxation in macromolecules. 2. Analysis of experimental results, *J. Am. Chem. Soc. 104*, 4559−4570.
62. Clore, G. M., Szabo, A., Bax, A., Kay, L. E., Driscoll, P. C., and Gronenborn, A. M. (1990) Deviations from the simple 2-parameter model-free approach to the interpretation of ^{15}N nuclear magnetic-relaxation of proteins, *J. Am. Chem. Soc. 112*, 4989−4991.
63. Fischer, M. W. F., Zeng, L., Majumdar, A., and Zuiderweg, E. R. P. (1998) Characterizing semilocal motions in proteins by NMR relaxation studies, *Proc. Natl. Acad. Sci. U.S.A. 95*, 8016−8019.
64. Pang, Y., Buck, M., and Zuiderweg, E. R. P. (2002) Backbone dynamics of the ribonuclease binase active site area using multinuclear (^{15}N and (CO)-^{13}C) NMR relaxation and computational molecular dynamics, *Biochemistry 41*, 2655−2666.
65. Wang, L. C., Pang, Y. X., Holder, T., Brender, J. R., Kurochkin, A. V., and Zuiderweg, E. R. P. (2001) Functional dynamics in the active site of the ribonuclease binase, *Proc. Natl. Acad. Sci. U.S.A. 98*, 7684−7689.
66. Vamvaca, K., Vogeli, B., Kast, P., Pervushin, K., and Hilvert, D. (2004) An enzymatic molten globule: Efficient coupling of folding and catalysis, *Proc. Natl. Acad. Sci. U.S.A. 101*, 12860−12864.
67. Fischer, M. W. F., Zeng, L., Pang, Y. X., Hu, W. D., Majumdar, A., and Zuiderweg, E. R. P. (1997) Experimental characterization of models for backbone picosecond dynamics in proteins. Quantification of NMR auto- and cross-correlation relaxation mechanisms involving different nuclei of the peptide plane, *J. Am. Chem. Soc. 119*, 12629−12642.
68. Wang, T. Z., Cai, S., and Zuiderweg, E. R. P. (2003) Temperature dependence of anisotropic protein backbone dynamics, *J. Am. Chem. Soc. 125*, 8639−8643.
69. Kast, P., AsifUllah, M., Jiang, N., and Hilvert, D. (1996) Exploring the active site of chorismate mutase by combinatorial mutagenesis and selection: The importance of electrostatic catalysis, *Proc. Natl. Acad. Sci. U.S.A. 93*, 5043−5048.
70. MacBeath, G., Kast, P., and Hilvert, D. (1998) A small, thermostable, and monofunctional chorismate mutase from the archeon *Methanococcus jannaschii*, *Biochemistry 37*, 10062−10073.
71. Guntert, P., Dötsch, V., Wider, G., and Wüthrich, K. (1992) Processing of multidimensional NMR data with the new software prosa, *J. Biomol. NMR 2*, 619−629.
72. Bartels, C., Xia, T. H., Billeter, M., Guntert, P., and Wüthrich, K. (1995) The program Xeasy for computer-supported NMR spectral-analysis of biological macromolecules, *J. Biomol. NMR 6*, 1−10.
73. Salzmann, M., Pervushin, K., Wider, G., Senn, H., and Wüthrich, K. (1999) [^{13}C]-constant-time [^{15}N,^{1}H]-TROSY-HNCA for sequential assignments of large proteins, *J. Biomol. NMR 14*, 85−88.
74. Salzmann, M., Wider, G., Pervushin, K., Senn, H., and Wüthrich, K. (1999) TROSY-type triple-resonance experiments for sequential NMR assignments of large proteins, *J. Am. Chem. Soc. 121*, 844−848.
75. Zhu, G., and Bax, A. (1990) Improved linear prediction for truncated signals of known phase, *J. Magn. Reson. 90*, 405−410.
76. Renner, C., Schleicher, M., Moroder, L., and Holak, T. A. (2002) Practical aspects of the 2D ^{15}N5-{^{1}H}-NOE experiment, *J. Biomol. NMR 23*, 23−33.
77. Mandel, A. M., Akke, M., and Palmer, A. G. (1995) Backbone dynamics of *Escherichia coli* ribonuclease HI: Correlations with structure and function in an active enzyme, *J. Mol. Biol. 246*, 144−163.
78. Palmer, A. G., Rance, M., and Wright, P. E. (1991) Intramolecular motions of a zinc finger DNA-binding domain from Xfin characterized by proton-detected natural abundance ^{12}C heteronuclear NMR spectroscopy, *J. Am. Chem. Soc. 113*, 4371−4380.
79. Kay, L. E., Torchia, D. A., and Bax, A. (1989) Backbone dynamics of proteins as studied by ^{15}N inverse detected heteronuclear NMR spectroscopy: Application to staphylococcal nuclease, *Biochemistry 28*, 8972−8979.
80. Orekhov, V. Y., Pervushin, K. V., Arsenviev, A. S. (1995) Backbone dynamics of (1−71) bacteriorhodopsin studied by 2D ^{1}H-^{15}N NMR spectroscopy, *Eur. J. Biochem. 219*, 887−896.

BI0474259